

Research Article

Rapid Photocatalytic Degradation of Pollutant from Water under UV and Sunlight via Cellulose Nanofiber Aerogel Wrapped by TiO₂

Song Li ¹, Xiaofeng Hao,² Xiangdong Dai ¹ and Tao Tao ²

¹College of Furniture and Art Design, Central South, University of Forestry and Technology, Changsha 410004, China

²Material Science and Engineering College, Central South, University of Forestry and Technology, Changsha 410004, China

Correspondence should be addressed to Xiangdong Dai; daixiangdong2000@163.com and Tao Tao; taotaohunter@163.com

Received 31 January 2018; Revised 7 April 2018; Accepted 16 April 2018; Published 17 July 2018

Academic Editor: Xin Jin

Copyright © 2018 Song Li et al. This is an open access article distributed under the Creative Commons Attribution License, which permits unrestricted use, distribution, and reproduction in any medium, provided the original work is properly cited.

Semiconductor photocatalysis can be used to decompose various organic compounds in open air under aqueous conditions with solar energy. A cellulose nanofiber/TiO₂ aerogel (CNFT) for rapid photocatalytic degradation of methylene blue (MB) solution was successfully fabricated through a facile hydrothermal method. TiO₂ nanoparticles adhered to the surface of cellulose nanofibers as scaffold through a hydrogen bond and were well-distributed. The particle size distribution data showed that the mean diameter of TiO₂ nanoparticles was around 6.8 nm. In the system of the as-prepared CNFT, CNF played important roles in adsorption of pollutant and in stopping the electron hole derived from TiO₂ from recombining. The composite aerogel exhibited efficient photocatalytic activity in the degradation of pollutant (MB) under ultraviolet light (UV) and sunlight irradiation. The composite aerogel could be regarded as a green and portable photocatalyst, because it was promising for wastewater treatment application as a result of its good high photocatalytic activity and stability under ultraviolet light and sunlight irradiation.

1. Introduction

With the urgency of water pollution, much attention was paid to the treatment of water pollution. Nowadays, the most commonly purified systems were employing filters packed with adsorbents like activated carbon, which do not constitute a definite conversion solution, merely transferring the pollutant to a different phase, thus requiring periodic maintenance and producing considerable amounts of waste. To prevent health hazard effects of water pollutions, urgent and new countermeasures must be implemented. The development of an efficient, green, and low-cost method for the removal of water pollutant compounds was essential. Photocatalysis continues to develop as a promising alternative technology for the renewal of our water system.

With its high photoreactivity, biological and chemical inertness, cost effectiveness, nontoxicity, and long-term stability against corrosion, TiO₂ was widely used as a

photocatalyst in wastewater treatment. [1]. Many organic pollutants, such as alcohols [2], phenols [3], dye [4], and carboxylic acids [5], can be photodegraded by TiO₂ nanoparticles under ultraviolet light (UV) or visible light irradiation. In the process of degradation, oxidation reactions allow the destruction of organic pollutants mainly through reactions with reactive oxygen species, such as hydroxyl radicals [6], which turn to be CO₂ and H₂O. The main photocatalytic procedure was the creation of electron-hole pairs interacting with the radiation, which were subsequently separated to be utilized in reduction and oxidation steps based on TiO₂ catalysts [7]. However, the practical applications of TiO₂ were still challenging in terms of their poor photocatalytic efficiency due to unwanted recombination of the electron-hole pairs [8]. In order to increase the photocatalytic activity, many researches had been conducted, for example, doping with nonmetallic atoms (namely S, N, P, etc.) [9], transition metals (namely, Pt,

Cu, Mg, etc.) [10], and polymers [11], or codoping with several ions.

Aerogels are highly porous materials that can have extremely low densities, large open pores, and low thermal transport, which can be applied in multiple fields such as catalysis [12, 13], superadsorbents, and desalination [13]. Most aerogels are fabricated from silica, metal oxides, pyrolyzed organic polymers, and carbon-based materials [14]. However, the traditional aerogels suffer from poor mechanical robustness, which has led to numerous attempts to overcome this problem. Several nanomaterials including carbon nanotubes [15, 16], carbonaceous nanofibers [17], and graphene [18, 19] have been recently developed as building blocks in the assembly of strong aerogels. Among them, cellulose nanofiber (CNF) from natural plants has attracted considerable attention because of its low density, high specific area, low thermal conductivity, and low dielectric permittivity [20]. CNF could be isolated from biomass materials [21]. The long and entangled CNF of cellulose I crystal type can form a strong aerogel network because of its fibrillar morphology and strong mutual hydrogen bonds, which facilitate mechanical ductility and flexibility of the aerogels [22, 23]. Potential applications of nanometer-sized cellulose included tissue engineering [24], efficient catalysts [25], electrooptical films [26], biodegradable packaging materials [27], nanofiber-reinforced composites [28], gas-barrier films [29], cosmetics [30], and other high-tech and high-performance materials. The research of inorganic nanoparticles/cellulose composite materials was a very exciting research area currently such as electrical [31], magnetic [32], and optical [33] properties. Because they have distinct size-dependent physicochemical and optoelectronic properties, the inorganic nanoparticles/cellulose composite materials could be considered as a candidate for the improvement of stability, retaining of the special morphology, and control of the growth of nanoparticles. The CNF aerogels have been used as templates for inorganic MnO_2 nanosheets [34] and $\text{Na}_2\text{Ti}_3\text{O}_7$ nanoparticles [35] and further functionalized to achieve ideal highly efficient water purification.

In this study, a cellulose nanofiber/ TiO_2 (CNFT) aerogel for rapid photocatalytic degradation of methylene blue in water was successfully fabricated through a facile hydrothermal method. In the system of the CNFT composite, TiO_2 nanoparticles could be adhered to wet CNF as a scaffold [36]. And the functionality of photodegradation could be enhanced through a synergistic interaction between the CNF and TiO_2 nanoparticles due to interactive structures in materials.

2. Materials and Methods

2.1. Materials. The bamboo was obtained from the bamboo forest of Zhejiang A&F University. Tetrabutyl titanate, titanium dioxide (P25), urea, citric acid, methylene blue, and other chemicals were of analytical grade. All the chemicals were used as received. Deionized water was used in all experiments.

2.2. Preparation of the CNFT Composite Aerogel. A CNF solution was prepared by the method of chemical

pretreatment combined with ultrasonic treatment, and the CNF from bamboo was referred to Xiao et al [37] and used for characterization. 100 mg CNF was put into 100 ml deionized water, and then a few milliliters of tetrabutyl titanate, 0.6 g urea, and 4 g citric acid were added with magnetic stirring for 30 min at room temperature. Subsequently, the mixtures were transferred to a Teflon-lined stainless-steel autoclave. The autoclave was placed in an oven and heated at 180°C for 24 h. The suspension was cooled down naturally and washed by a centrifuge treatment with 6000 rpm/s for 5 min. To obtain the homogeneous solution, the bulk after centrifuge treatment was put into deionized water and then underwent an ultrasonic treatment for 1 min with an output power of 50 W in an ice water bath to disperse the solution. The obtained concentrated suspension, with a high viscosity and gel-like appearance, was freeze-dried at -55°C at $10\ \mu\text{Pa}$ for 60 h. The lightweight, solid, and sponge-like aerogel was produced. The volume of tetrabutyl titanate was 1 ml, 2 ml, and 4 ml and was coded as CNFT1, CNFT2, and CNFT4, respectively.

2.3. Characterization. The morphological feature of the CNF and CNFT composite was observed using a scanning electron microscope (SEM, FEI, Quanta 200, USA) and transmission electron microscope (TEM, FEI, Tecnai G20, USA). Crystal-line structures were identified by X-ray diffraction technique (XRD, Rigaku, D/Max 2200, Japan) operating with Cu $K\alpha$ radiation ($\lambda = 1.5418\ \text{\AA}$) at a scan rate (2θ) of 2°min^{-1} and the accelerating voltage of 40 kV and the applied current of 30 mA ranging from 5° to 90° . The X-ray photoelectron spectroscopy (XPS, ULVAC-PHI Inc., Japan) analysis of the specimen was carried out using a microfocused (100 lm, 25 W, 15 kV) monochromatic Al- $K\alpha$ source ($h\nu = 1486.6\ \text{eV}$), a hemispherical analyzer, and a multichannel detector. Thermal-physical properties of the CNF and CNFT composite were simultaneously assessed with a Hot Disk TPS 2500 S instrument (Hot Disk AB) using 20 mW output power in the transient mode from 25°C to 800°C , with a heating rate of $10^\circ\text{C}\cdot\text{min}^{-1}$ under nitrogen atmosphere. FTIR spectra were recorded on a Fourier transform infrared instrument (Magna 560, Nicolet, Thermo Electron Corp.) in the range of $400\text{--}4000\ \text{cm}^{-1}$ with a resolution of $4\ \text{cm}^{-1}$. UV-Vis spectra were recorded on a TU-9001 spectrophotometer equipped with a Labsphere diffuse reflectance accessory. The Brunauer-Emmett-Teller (BET) surface areas were measured by nitrogen adsorption isotherm measurements at 77 K on a JW-BK instrument.

2.4. Photocatalytic Activity. The photocatalytic activities of CNF, P25, TiO_2 synthesized at similar conditions without adding cellulose nanofiber, and CNFT were measured by the photodegradation of methylene blue as model reaction under UV and sunlight illumination. Typically, six groups of 10 mg of the prepared CNFT composites were dipped in 50 ml MB solution (15 ppm). The mixture solution was then exposed to UV irradiation produced by a tunable high-pressure Hg lamp with the main peak at a wavelength of 365 nm. 10 ml of suspension was extracted afterwards per 5 min from one of the six groups and then

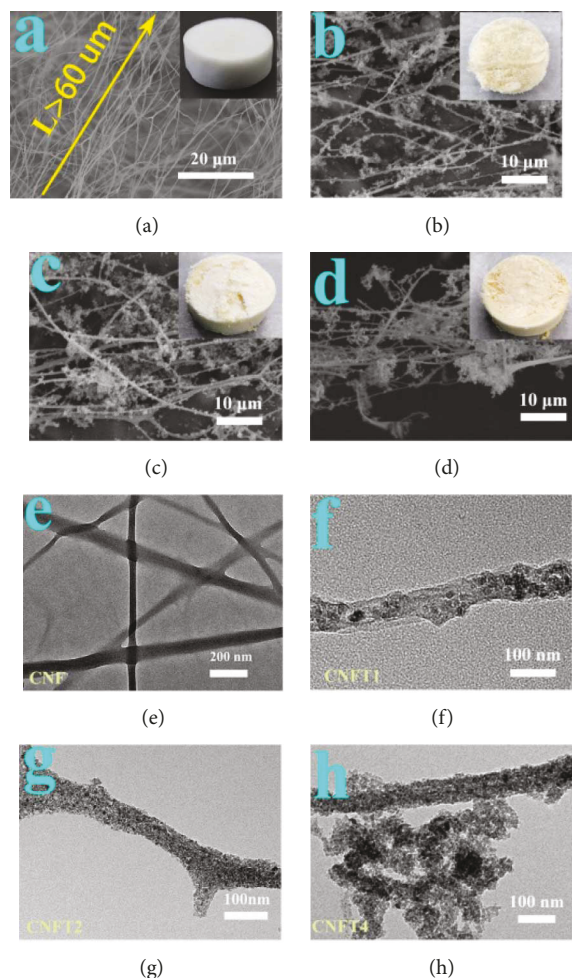


FIGURE 1: The morphologies of CNF and CNFT. (a)–(d) The SEM micrographs of CNF, CNFT1, CNFT2, and CNFT4, respectively, and the shape in the inset. (e)–(h) The TEM images of CNF, CNFT1, CNFT2, and CNFT4, respectively.

centrifuged at 6000 rpm for 5 min to get rid of the CNFT from the supernatant. Samples were exposed to sunlight. The selected exposure time was 1 h every day from 1 p.m. to 2 p.m. on sunny days. Then, the solution was analyzed by recording the UV–Vis spectrum of MB at the maximum absorbance of 664 nm. The degradation of MB was studied with UV visible spectroscopy measurement carried out on a UV visible spectrophotometer (model Tu-1901) in the range of 450–750 nm. The normalized temporal concentration changes (C/C_0) of MB during the photodegradation were proportional to the normalized maximum absorbance (A/A_0) and derived from the changes in the dye's absorption profile (664 nm) at a given time interval. The photodegradation rate was calculated by the following equation:

$$\text{Photodegradation rate} = \frac{(C_0 - C)}{C_0} \times 100\%, \quad (1)$$

where C is the concentration of MB solution at time and C_0 is the initial concentration.

3. Results and Discussion

Figure 1 shows the morphologies of CNF and CNFT. After water was completely removed through freeze-drying, a light-weight sponge-like aerogel was produced which did not have any collapse with the density of $1 \text{ mg}\cdot\text{cm}^{-3}$. As shown in Figure 1(a), the macroscopic morphology of the CNF aerogel was white with integrity and had a well-defined shape. The SEM image showed the micromorphology image of the CNF fibrils; the length of CNF fibrils was much longer than $60 \mu\text{m}$. From Figures 1(b)–1(d), it shows the SEM images of CNFT1, CNFT2, and CNFT4, which possessed an interconnected 3D network microstructure. The shapes are shown in the inset. They were turned to be beige from white CNF aerogel because of the formation of TiO_2 nanoparticles in the samples inside. After modification by TiO_2 nanoparticles, the structure of the CNFT2 composite showed filamentous fibers covered by nanoparticles. Figure 1(e) shows TEM images of CNF samples, which exhibited some slender fibrils with an average diameter of the CNF fibrils of about 63.2 nm. The CNF exhibited a high draw ratio about 1000 according to the length referred before. The TEM images of

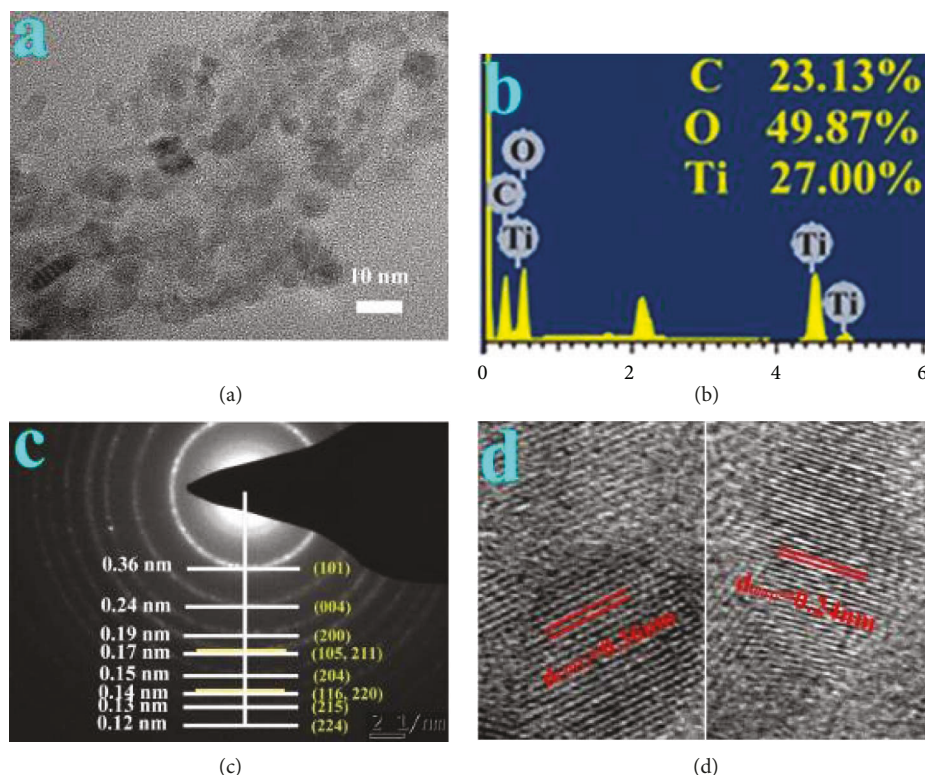


FIGURE 2: (a) The enlarged view of the TEM image, (b) the EDX spectra, (c) selected area electron diffraction, and (d) high-resolution TEM image, of CNFT2.

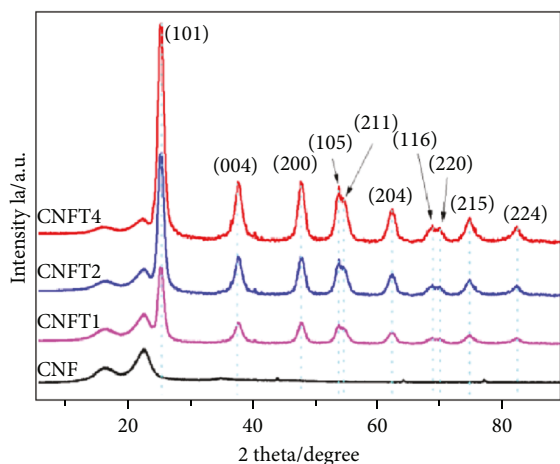


FIGURE 3: XRD patterns of (a) CNF and (b) CNFT.

samples CNFT1, CNFT2, and CNFT4 are shown in Figures 1(f)–1(h). The surface of CNFT4 was wrapped by TiO_2 nanoparticles in the surface of fibers, which was denser than that of CNFT2. With more and more TiO_2 nanoparticles formed, the CNF was not able to contain these particles so that some of TiO_2 particles were outside of the fibers. In CNFT2, the TEM images of the sample showed that a large quantity of TiO_2 nanoparticles were formed like a film structure and coated on the surface of the CNF fibrils. Furthermore, the TiO_2 nanoparticles were well-distributed. In terms of CNFT1, TiO_2 nanoparticles were interspersed basically in the surface of the cellulose fibers.

Figure 2(a) is the enlarged view of CNFT2; the particle size distribution data showed that the mean diameter of TiO_2 nanoparticle sizes was around 6.8 nm. The energy-dispersive spectrum (EDS) in Figure 2(b) indicates that there were C, O, and Ti elements in the composite sample, suggesting that the TiO_2 nanoparticles had been synthesized in the composite aerogel. Figure 2(c) shows the SAED pattern, in which eight main diffraction rings correspond to the (101), (004), (200), (105, 211), (204), (116, 220), (215), and (224) planes of polycrystalline TiO_2 with a spherical structure. Besides, the diffraction rings were discontinuous and consist of rather sharp spots, indicating that the nanoparticles were well crystallized. To further investigate the distribution of TiO_2 particles, the HRTEM image was displayed as shown in Figure 2(d). The results clearly revealed a lattice fringe with a d-spacing of 0.36 nm and 0.24 nm corresponding to the (101) and (004) planes, which were present in anatase phase TiO_2 .

The phase structures of CNF and CNFT were revealed by XRD analysis. As shown in Figure 3, it was clear that diffraction peaks at 16.5° (101) and 22.5° (002) were typical cellulose peaks [38]. The CNF clearly retained the cellulose structure, indicating that the CNF was prepared successfully by isolating from the raw material bamboo. The diffraction peaks of CNFT composite samples were observed at 25.2° , 37.7° , 47.8° , 53.8° , 55.0° , 62.7° , 68.7° , 70.3° , 74.9° , and 82.6° , which corresponded to planes (101), (004), (200), (105), (211), (204), (116), (220), (215), and (224) [39], respectively. It was clear that diffraction peaks in the XRD pattern were well indexed to the anatase phase of TiO_2 . The prepared TiO_2 also

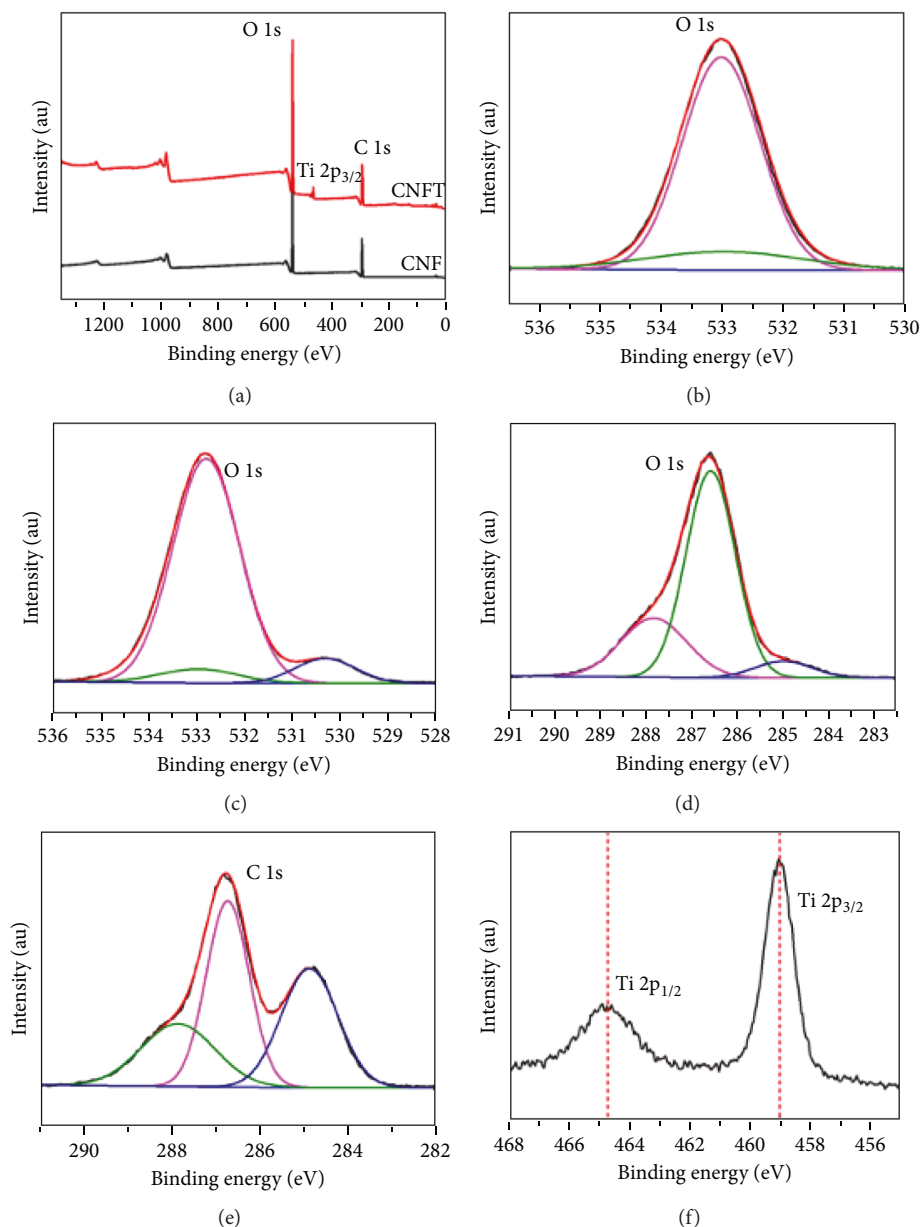


FIGURE 4: (a) A full-scan XPS spectra of CNF and CNFT, high-resolution XPS spectra of (b, c) O 1s of CNF and CNFT, (d, e) C 1s of CNF and CNFT, and (f) Ti 2p of CNFT.

exhibited excellent crystallinity for the high and narrow peaks in the XRD patterns.

Figure 4 shows the XPS spectra of the CNF and CNFT2. The wide scan spectra of the CNF exhibited two major peaks with binding energy at 286.1 eV and 532.1 eV corresponding to the C 1s and O 1s of CNF, respectively. However, in CNFT2, an additional peak was observed at a binding energy of 458.1 eV corresponding to the Ti 2p of TiO_2 [40]. The high-resolution XPS spectra were examined in order to research the structure further. As shown in Figure 4(b), two peaks were observed at 533 eV in the high-resolution spectra of O 1s in CNF. Another peak was observed at 530.3 eV in the high-resolution spectra of O 1s in CNFT2 except the two peaks in the high-resolution spectra of O 1s in the CNF at the same location. The additional peak could be attributed

to O-Ti^{4+} . This further confirmed the presence of TiO_2 in CNFT2. In both of the samples, three peaks were observed for C 1s in Figures 4(d) and 4(e) at the same location. The differences in the same peak on intensity at 285 eV were attributed to C-C; the results may be some degradation during hydrothermal treatment. Furthermore, the binding energies of Ti 2p_{3/2} and Ti 2p_{1/2} appear at 459.02 and 464.92 eV, respectively (Figure 4(f)), which can be well attributed to the Ti^{4+} in bulk TiO_2 [41]. According to the above results, it was obvious that TiO_2 would have to be produced in CNFT successfully.

Figure 5 shows the different phase thermogravimetric and differential thermal analysis (TG-DTA) curves of CNF and CNFT2. In this study, the process of sample pyrolysis was divided into three stages, corresponding to drying (stage 1)

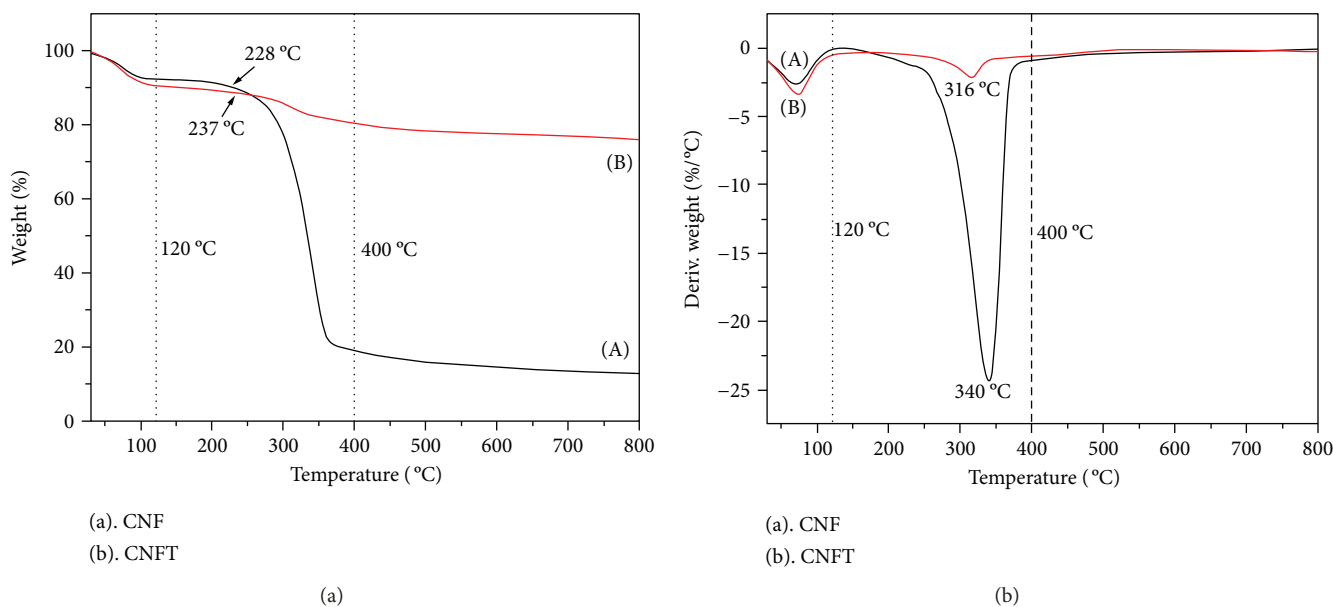


FIGURE 5: TGA and DTG thermograms of (a) CNF and (b) CNFT2 under nitrogen atmosphere.

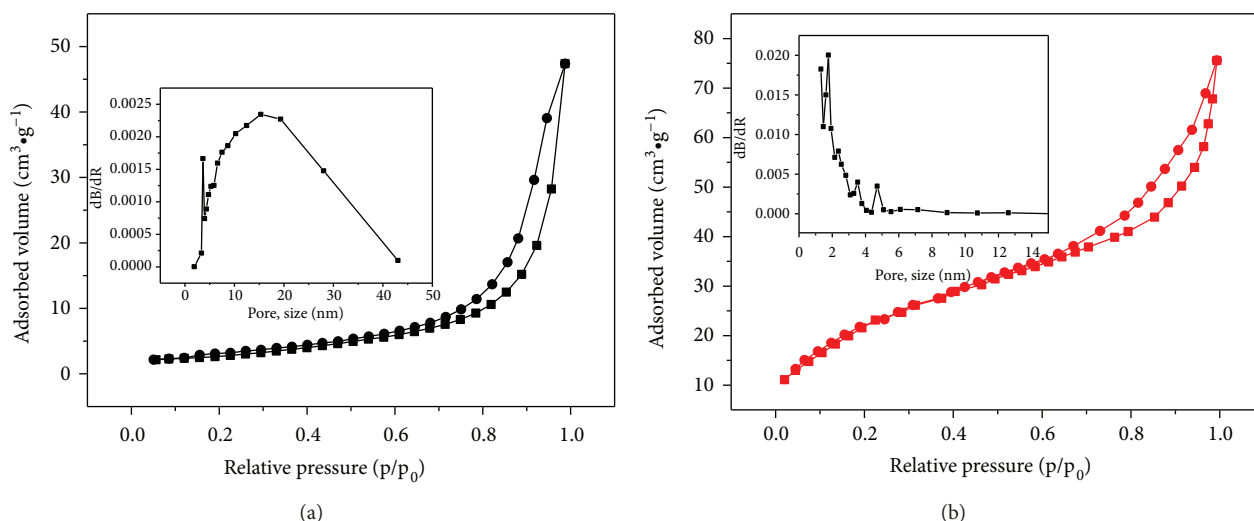


FIGURE 6: N_2 adsorption/desorption isotherms of (a) CNF and (b) CNFT2 aerogels and corresponding pore size distribution derived from the adsorption branch [43].

TABLE 1: Texture properties of CNF and CNFT2.

Sample	S_{BET} ($m^2 \cdot g^{-1}$)	V_{total} ($cm^3 \cdot g^{-1}$)	Average pore diameter (nm)
CNF	10.1	0.073	29.3
CNFT2	85.6	1.169	5.5

and pyrolysis (stage 2 and 3). In the first stage, a small mass (7%–9%) loss was observed in the temperature range of 25–120°C, which due to the evaporation of water molecules in the materials or low molecular weight compounds for temperature increased. In the second stage (120–400°C), some flat lines at the TG/DTG curves were displayed, and the beginning of weight loss of the main degradation step was observed at 228°C and 237°C, corresponding to the curves of CNF and

CNFT2, respectively. Then, values (TG curve) of the samples decreased sharply with time. Importantly, the different components of CNF and CNFT2 caused great differences on the DTG curves. The rate of degradation reached its peak at 340°C and 316°C for CNF and CNFT2, respectively. The reason for this phenomenon may be attributed to the deposition of the TiO_2 particles on the wood surface. Combining strongly with TiO_2 particles via electrostatic attraction and hydrogen bond, the pyrolysis rate of CNFT2 decreased nearly tenfold as much as that of CNF, which effectively enhanced the thermal stability of CNFT2 [42]. In the third stage, the TG curves of CNF and CNFT2 were relatively flat. This result indicated that all the samples were degraded completely.

The N_2 adsorption/desorption isotherms of CNF and CNFT2 aerogels displayed a direct hysteresis loop, shown

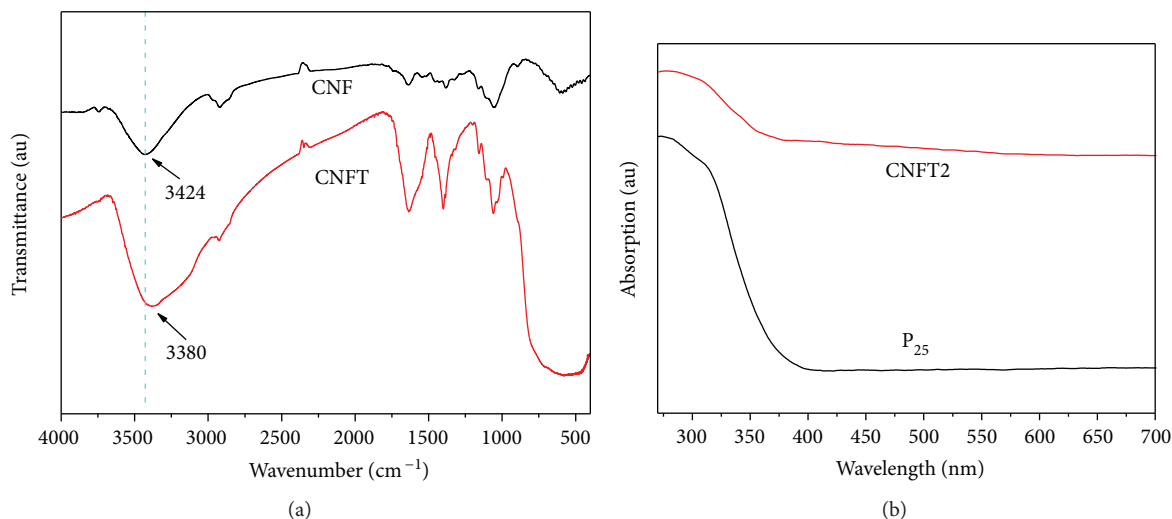


FIGURE 7: (a) FT-IR spectra of the CNF and CNFT2. (b) UV-Vis spectra of P25 and CNFT2.

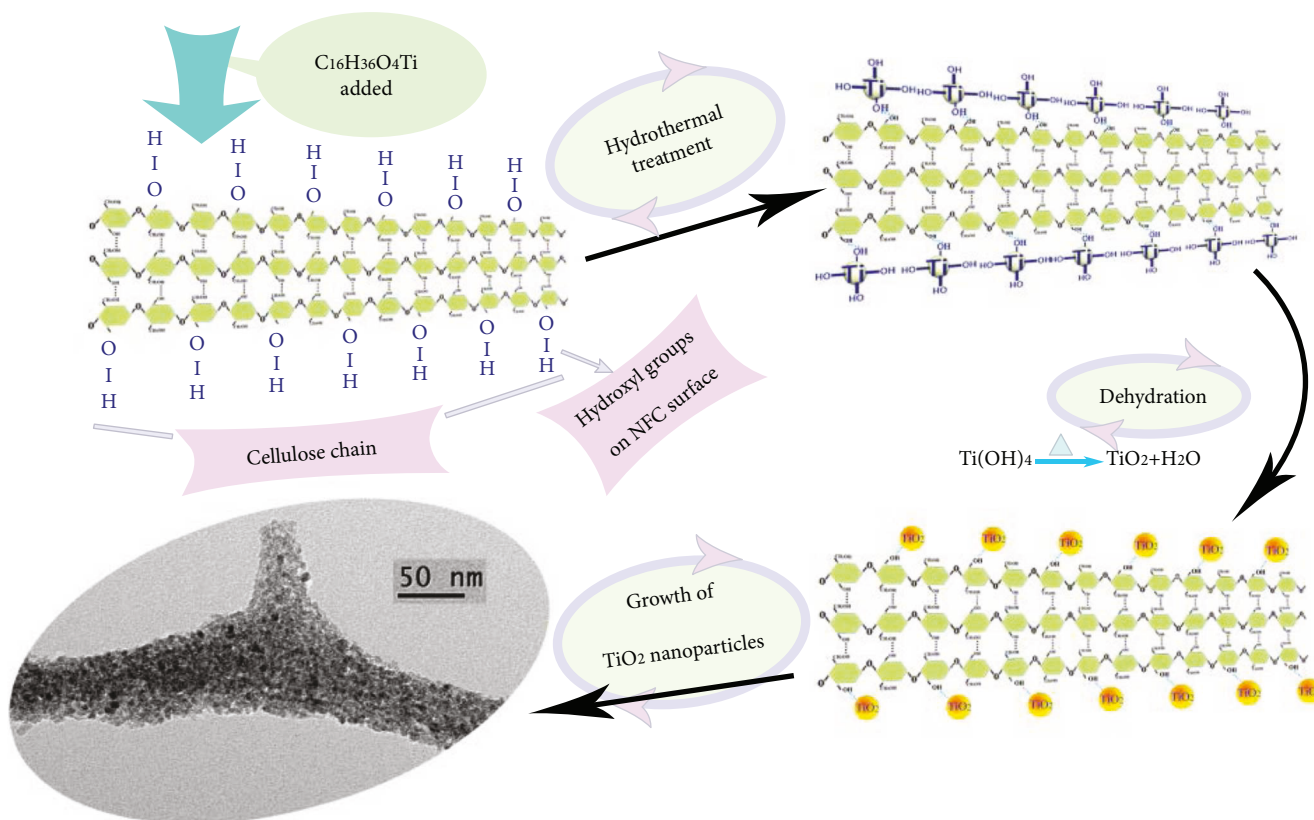


FIGURE 8: Mechanism for the generation of the TiO_2 nanoparticles on the surface of CNF.

in Figure 6, belonging to type IV (according to IUPAC classification), which were consistent with the results researched by Fan et al.'s group [43]. The results reflected the presence of a mesoporous structure in the samples. The corresponding pore size distribution of the samples was calculated by the BJH method and was illustrated in the inset of Figure 6. The CNFT2 showed a smaller pore diameter (dominated in about 2 nm) than did CNF (dominated about 15 nm), but it also exhibited a sharper and more

concentrated peak. The porosity detailed data of CNF and CNFT2 is summarized in Table 1. It could be seen that the specific surface of CNFT2 was 8 times higher than that of CNF, and the pore volume of CNFT2 was 2 orders of magnitude above that of CNF.

Figure 7(a) shows the FT-IR spectra of CNF and CNFT2. The dominant peak of CNF in the region around 3424 cm^{-1} was attributed to stretching vibrations of hydroxyl groups of cellulose. However, in CNFT2, the peak at 3380 cm^{-1}

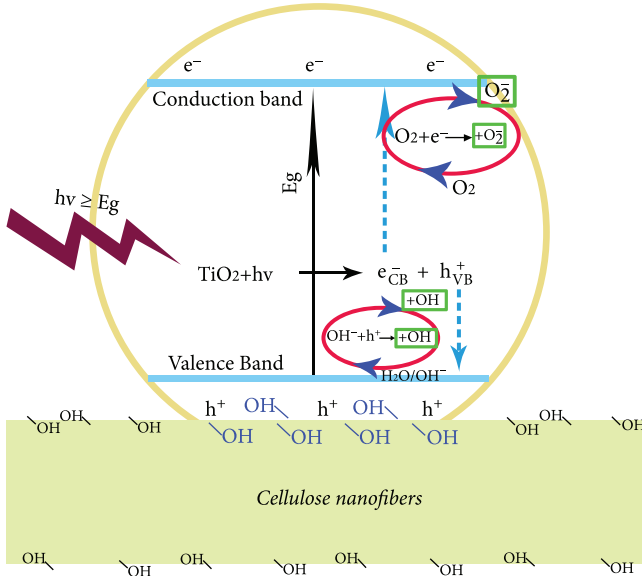


FIGURE 9: Schematic illustrating the strategies to develop $\bullet\text{O}_2^-$ and $\bullet\text{OH}$.

was shifted to lower wavenumbers, indicating a strong interaction between the hydroxyl groups of cellulose and TiO_2 nanoparticles through a hydrogen bond [44]. This strong interaction led to TiO_2 nanoparticles adhering to the surface of CNF. Figure 7(b) shows the UV-Vis spectra of P25 and CNFT2. An obvious red shift could be observed on the cut-off wavelength from 385 to 411 nm of CNFT2, compared to P25. The result indicated the band gap of CNFT2 triggered by hydrogen bonds between P25 and CNF. The band gap energy (E_g) was obtained according to [45]

$$E_g = h \cdot \frac{C}{\lambda}, \quad (2)$$

where h = plank constant = 6.626×10^{-34} joules/sec, C = speed of light = 3.0×10^8 meters/sec, λ = cut-off wavelength at $1 \text{ eV} = 1.6 \times 10^{-19}$ joules. For CNFT2, the band gap energy about 3.023 eV was lower than that of the standard commercial P25 (3.227 eV), indicating that CNFT2 was able to absorb photons not only from UV irradiation but also from visible light. The extended light absorption range made the CNFT2 composites good candidates for visible light photocatalysis.

The interaction of TiO_2 nanoparticles and the surface of CNF are shown in Figure 8. As we all know, there were plenty of hydroxyl groups present on the surface of CNF [46]. When $\text{C}_{16}\text{H}_{36}\text{O}_4\text{Ti}$ was added in the solution, $\text{Ti}(\text{OH})_4$ could generate due to the hydrolysis of $\text{C}_{16}\text{H}_{36}\text{O}_4\text{Ti}$. $\text{Ti}(\text{OH})_4$ molecules could be interacted with the surface of CNF by the hydrogen bond between the hydroxyl groups on the surface of CNF and the hydroxyl groups of $\text{Ti}(\text{OH})_4$, which was consistent with the result of the FT-IR. On dehydration, TiO_2 could be generated through losing H_2O among the hydroxyl groups in $\text{Ti}(\text{OH})_4$. TiO_2 and CNF would be combined together due to the existence of hydrogen bonds between the hydroxyl groups on the surface of TiO_2 and CNF. This further helped

in the generation of the TiO_2 nuclei on the surface of the CNF. As the reaction proceeded, the nuclei would grow and form TiO_2 nanoparticles on the surface of the CNF.

Figure 9 illustrates the detailed performance of the photodegradation procedure of CNFT. The basic species responsible for the photodegradation of any pollutant were hydroxyl radicals and anion radical superoxide. Electron (e_{CB}^-) and hole (h_{VB}^+) pairs with excited high-energy states occurred when wide band gap semiconductors were irradiated higher than their band gap energy [47]. Firstly, the excitation of electrons from the valance band to the conduction band by the photons emanated from the UV source, and then the holes generated due to the excitation process acted as a decomposing agent or combined with the surface hydroxyl species on the TiO_2 to form the hydroxyl radical. h_{VB}^+ and e_{CB}^- were powerfully oxidizing. h_{VB}^+ reacted with OH^- contained in water resulting in their oxidation producing $\bullet\text{OH}$. e_{CB}^- could be reacted with O_2 forming an anion radical superoxide. The organic compounds were oxidized to CO_2 and H_2O . However, it should be noted that the continuous reactions during photocatalytic degradation were attributed to the presence of dissolved oxygen and water molecules [48]. Cellulose played an important role in the CNFT composite when the procedure of photodegradation was conducted. It would provide innumerable hydroxyl groups on the surface, which could capture the holes and stop the electron-hole from recombining. The electron and hole pairs could be separated to conduce and continue the reaction of oxidation.

Figure 10 shows the performance of photodegradation of the CNFT composite. TiO_2 had great potential application in environmental protection. In this study, the potential application of CNFT was investigated to degrade dye under UV light and sunlight. Methylene blue (MB) was chosen as a model dye. The time-dependent UV-Vis optical absorption of MB and its degradation by CNFT2 under UV light is shown in Figure 10(a). The inset shows the colorless MB aqueous solution under UV light as a function of time. MB solutions containing CNFT2 were degraded almost absolutely within 20 min. The colors faded gradually in solution for dye degradation with time. After 5 minutes, the color turned to be shallow and became colorless after about 20 minutes. It indicated that MB was degraded almost completely for about 20 minutes. The results were consistent with the relevant UV-Vis spectra as a function of time in the inset of Figure 10(a). In addition, the as-prepared aerogels (CNF and CNFTs) immersed in MB solution were compared in darkness (Figure 10(b)). It was observed that the decrease in absorption could be reasonable due to the adsorption on the surface. The decrease in absorption could result from adsorption on the surfaces of aerogels. However, the adsorption capacity of CNFT was higher than that of CNF because of the higher specific surface area. The results could conclude that CNFT possessed a special nanostructure and enhanced the dye adsorption. In contrast, UV light irradiation for 30 min is shown in Figure 10(c). A self-decomposition phenomenon of 14.8% could be seen in the MB solution without anything. About 27.5% of MB had been degraded in the case of CNF. However, the as-prepared CNFT exhibited much better photocatalytic activity. Moreover, the property of photodegradation of the composite

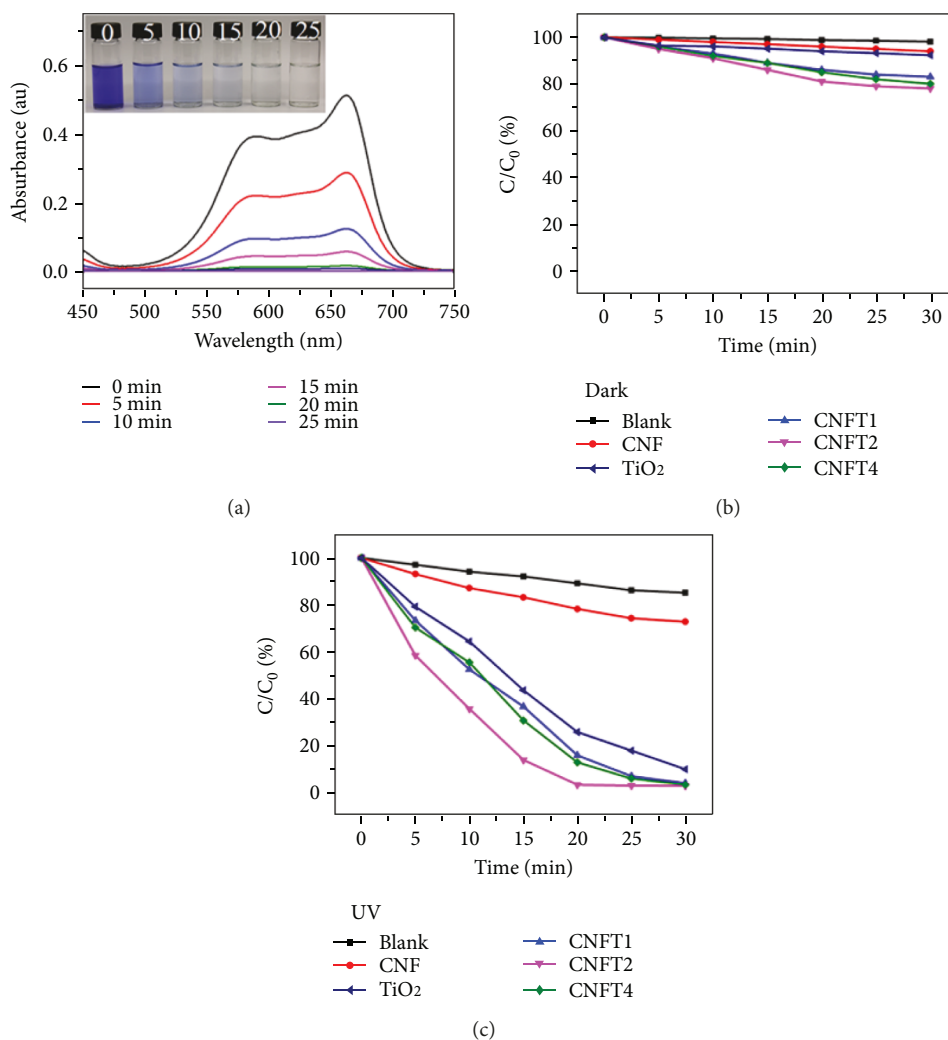


FIGURE 10: (a) Time-dependent UV–visible spectra of MB and its degradation by CNFT2 under UV irradiation; the colors in different times were shown in the inset. (b) Quantitative study of photocatalytic degradation of MB by blank, CNF, TiO₂, and as-prepared CNFT as a function in darkness and (c) under UV irradiation.

TABLE 2: Summary of results for degradation of MB employed by modified TiO₂ under UV light.

Photocatalyst	Modified type	Power (W)	Photodegradation rate (%)	Time (min)	Ref.
TiO ₂	Pd	300	98	60	[49]
TiO ₂	Ag ₂ O	160	97	360	[50]
TiO ₂	Fe ₂ O ₃	400	81	100	[51]
TiO ₂	Ag–Ag ₂ O	112	99.62	200	[52]
TiO ₂	Carbon nanotubes	125	76	200	[53]
TiO ₂	Cellulose	1000	98.1	20	This work
TiO ₂	Cellulose	500	96.7	45	This work
TiO ₂	Cellulose	200	89.6	200	This work

CNFT2 was better than the others. Contributing to the interaction of cellulose and TiO₂, 98.1% MB dye was degraded by the as-prepared CNFT2 only for 20 minutes, and 97% and 97.7% MB dye were degraded by CNFT1 and CNFT4 for 30 minutes. Furthermore, 92.3% MB dye was degraded by the as-prepared TiO₂ for 30 minutes. This observation would

suggest that CNFT could enhance the functionality through a synergistic interaction between the CNF and TiO₂ nanoparticles due to the interactive structure in materials. On the other hand, in order to increase the photocatalytic activity, many researches had been conducted in the previous investigation. The summary of results for MB degradation

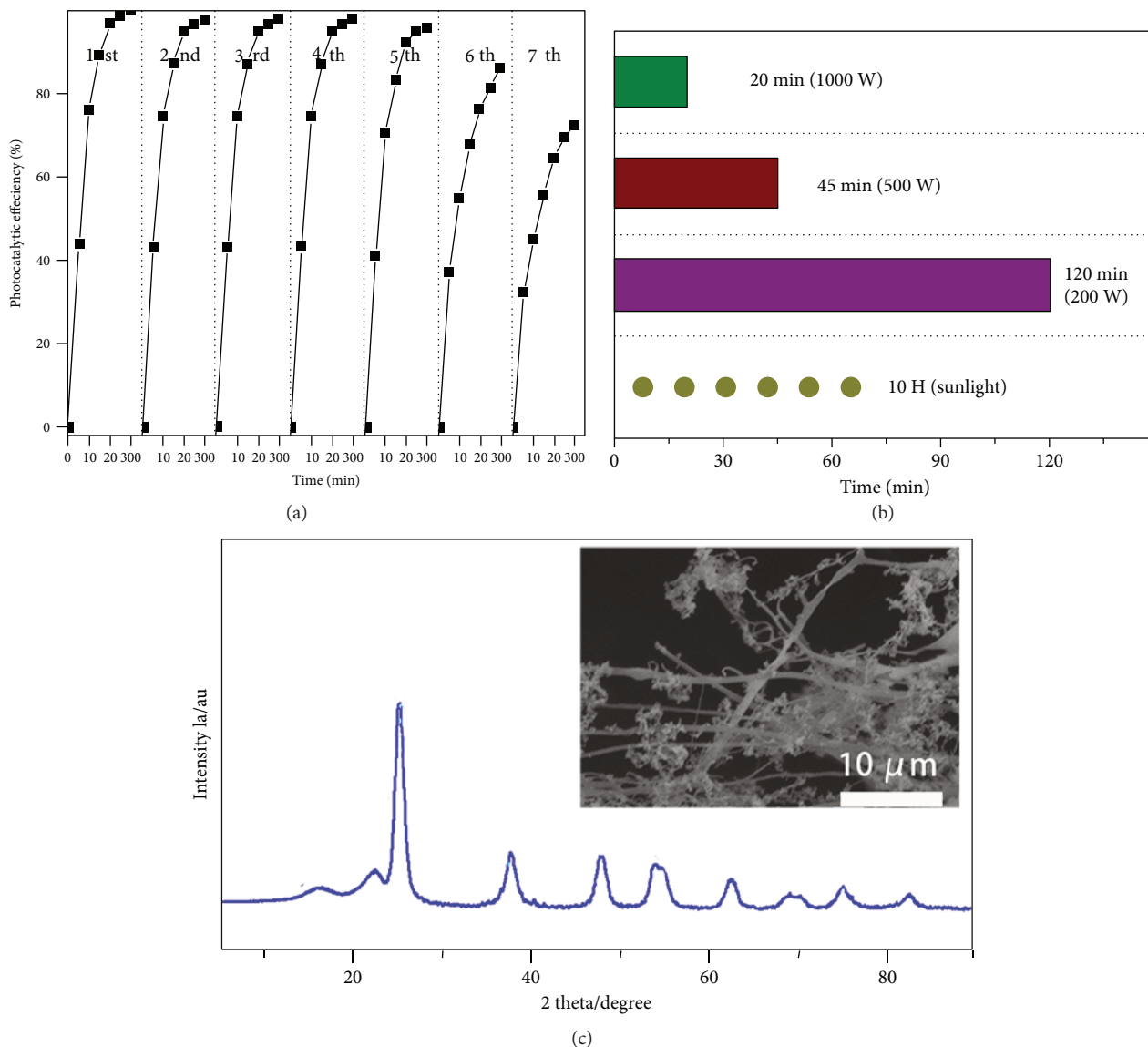


FIGURE 11: (a) Seven cycles of the photodegradation of MB using CNFT2 as a photocatalyst under UV irradiation for 30 min. (b) Degradation of MB with different light intensities of UV irradiation and sunlight. (c) XRD pattern and SEM image of the CNFT2 after the 7th recycle.

employed by modified TiO_2 with different components in different conditions is shown in Table 2.

The stability and reusability of the CNFT2, as a typical representative, were investigated and exhibited by performing several UV irradiation cycles. In each cycle, simulated UV light was irradiated for 30 min at room temperature in Figure 11(a). Obviously, CNFT2 could keep a superior photocatalytic performance with the degradation beyond 98% after 4 photocatalytic cycles. After the 7th photocatalytic recycle finished, the photodegradation of CNFT2 decreased to about 74%, which was due to about 19% mass loss of CNFT2 during the collection process. Hence, the decreased photocatalytic activity of CNFT2 after multiple cycles was contributed to the mass loss of CNFT2. Compared with other research results, CNFT2 showed an excellent stability and reusability. Furthermore, MB solution with CNFT2 was exposed to UV irradiation produced by a tunable pressure Hg lamp, at

1000 W, 500 W, and 200 W, and sunlight outdoor for 1 h in the noon every sunny day. Figure 11(b) shows that MB could be well degraded with different light intensities of UV irradiation and sunlight. The results indicated that CNFT2 exhibited excellent properties of photodegradation not only under UV irradiation but also under sunlight which could cause the MB to photodegrade. As shown in Figure 11(c), the results of the XRD pattern and SEM image of CNFT2 after the 7th recycle were not obviously different from that of CNFT2 before being used for photocatalytic reaction, which illustrated the stability of CNFT2.

4. Conclusions

Cellulose nanofiber/ TiO_2 aerogels were successfully fabricated, which the obtained TiO_2 nanoparticles adhered to the surface of the cellulose nanofiber as scaffold through a

hydrogen bond. The composites of CNFT were good enough for photocatalytic applications and even much better than CNF and individual TiO₂ nanoparticles. This observation would suggest that CNFT could enhance the functionality through a synergistic interaction between the CNF and TiO₂ nanoparticles due to the interactive structure in materials. The performance might lead to the fabrication of new materials that could be used for multiple activities ideal for water treatment applications as TiO₂ was non-toxic and efficient in preventing infections. Furthermore, the composite aerogel could be regarded as a green and portable photocatalyst because it was promising for wastewater treatment application as a result of its good high photocatalytic activity and stability under UV light irradiation. The one-step in situ method could be generalized to the incorporation of many more metal/metal oxide nanostructures in cellulose products.

Data Availability

The data used to support the findings of this study are available from the corresponding author upon request.

Conflicts of Interest

The authors declare that there are no conflicts of interest regarding the publication of this paper.

Acknowledgments

The work was financially supported by a project supported by the Natural Science Foundation of Hunan Province (Grant no. 2016JJ3185).

References

- [1] R. Fagan, D. McCormack, S. Hinder, and S. Pillai, "Photocatalytic properties of g-C₃N₄-TiO₂ heterojunctions under UV and visible light conditions," *Materials*, vol. 9, no. 4, pp. 286–291, 2016.
- [2] Q. Wang, M. Zhang, C. Chen, W. Ma, and J. Zhao, "Photocatalytic aerobic oxidation of alcohols on TiO₂: the acceleration effect of a Brønsted acid," *Angewandte Chemie International Edition*, vol. 49, no. 43, pp. 7976–7979, 2010.
- [3] Z. Liu, X. Zhang, S. Nishimoto et al., "Highly ordered TiO₂ nanotube arrays with controllable length for photoelectrocatalytic degradation of phenol," *The Journal of Physical Chemistry C*, vol. 112, no. 1, pp. 253–259, 2007.
- [4] A. T. Kuvarega, R. W. M. Krause, and B. B. Mamba, "Nitrogen/palladium-codoped TiO₂ for efficient visible light photocatalytic dye degradation," *Journal of Physical Chemistry C*, vol. 115, no. 45, pp. 22110–22120, 2011.
- [5] Q. Qu, H. Geng, R. Peng et al., "Chemically binding carboxylic acids onto TiO₂ nanoparticles with adjustable coverage by solvothermal strategy," *Langmuir*, vol. 26, no. 12, pp. 9539–9546, 2010.
- [6] K. Lv, J. Yu, K. Deng, X. Li, and M. Li, "Effect of phase structures on the formation rate of hydroxyl radicals on the surface of TiO₂," *Journal of Physics and Chemistry of Solids*, vol. 71, no. 4, pp. 519–522, 2010.
- [7] L. Karimi, M. E. Yazdanshenas, R. Khajavi, A. Rashidi, and M. Mirjalili, "Using graphene/TiO₂ nanocomposite as a new route for preparation of electroconductive, self-cleaning, antibacterial and antifungal cotton fabric without toxicity," *Cellulose*, vol. 21, no. 5, pp. 3813–3827, 2014.
- [8] J. Hofkens and M. B. J. Roeffaers, "Electrochemistry: photocatalysts in close-up," *Nature*, vol. 530, no. 7588, pp. 36–37, 2016.
- [9] H. Li, H. Liu, A. Fu et al., "Synthesis and characterization of N-doped porous TiO₂ hollow spheres and their photocatalytic and optical properties," *Materials*, vol. 9, no. 10, pp. 849–854, 2016.
- [10] H. Huang, H. Huang, L. Zhang, H. Peng, X. Ye, and D. Y. C. Leung, "Enhanced degradation of gaseous benzene under vacuum ultraviolet (VUV) irradiation over TiO₂ modified by transition metals," *Chemical Engineering Journal*, vol. 259, pp. 534–541, 2015.
- [11] J. Ren, S. Wang, C. Gao, X. Chen, W. Li, and F. Peng, "TiO₂-containing PVA/xylan composite films with enhanced mechanical properties, high hydrophobicity and UV shielding performance," *Cellulose*, vol. 22, no. 1, pp. 593–602, 2015.
- [12] C. Moreno-Castilla and F. J. Maldonado-Hódar, "Carbon aerogels for catalysis applications: an overview," *Carbon*, vol. 43, no. 3, pp. 455–465, 2005.
- [13] J. Biener, M. Stadermann, M. Suss et al., "Advanced carbon aerogels for energy applications," *Energy & Environmental Science*, vol. 4, no. 3, pp. 656–667, 2011.
- [14] W. Chen, Q. Li, Y. Wang et al., "Comparative study of aerogels obtained from differently prepared nanocellulose fibers," *ChemSusChem*, vol. 7, no. 1, pp. 154–161, 2014.
- [15] J. Zou, J. Liu, A. S. Karakoti et al., "Ultralight multiwalled carbon nanotube aerogel," *ACS Nano*, vol. 4, no. 12, pp. 7293–7302, 2010.
- [16] C. Wu, X. Huang, X. Wu, R. Qian, and P. Jiang, "Mechanically flexible and multifunctional polymer-based graphene foams for elastic conductors and oil-water separators," *Advanced Materials*, vol. 25, no. 39, pp. 5658–5662, 2013.
- [17] H.-W. Liang, Q.-F. Guan, L.-F. Chen, Z. Zhu, W.-J. Zhang, and S.-H. Yu, "Macroscopic-scale template synthesis of robust carbonaceous nanofiber hydrogels and aerogels and their applications," *Angewandte Chemie*, vol. 124, no. 21, pp. 5191–5195, 2012.
- [18] Z. Xu, Y. Zhang, P. Li, and C. Gao, "Strong, conductive, lightweight, neat graphene aerogel fibers with aligned pores," *ACS Nano*, vol. 6, no. 8, pp. 7103–7113, 2012.
- [19] S. Yin, Z. Niu, and X. Chen, "Assembly of graphene sheets into 3D macroscopic structures," *Small*, vol. 8, no. 16, pp. 2458–2463, 2012.
- [20] E. Abraham, B. Deepa, L. A. Pothan et al., "Physicomechanical properties of nanocomposites based on cellulose nanofibre and natural rubber latex," *Cellulose*, vol. 20, no. 1, pp. 417–427, 2013.
- [21] N. C. T. Martins, C. S. R. Freire, R. J. B. Pinto et al., "Electrostatic assembly of Ag nanoparticles onto nanofibrillated cellulose for antibacterial paper products," *Cellulose*, vol. 19, no. 4, pp. 1425–1436, 2012.
- [22] W. Chen, H. Yu, Q. Li, Y. Liu, and J. Li, "Ultralight and highly flexible aerogels with long cellulose I nanofibers," *Soft Matter*, vol. 7, no. 21, pp. 10360–10368, 2011.
- [23] M. Pääkkö, J. Vapaavuori, R. Silvennoinen et al., "Long and entangled native cellulose I nanofibers allow flexible aerogels

- and hierarchically porous templates for functionalities,” *Soft Matter*, vol. 4, no. 12, pp. 2492–2499, 2008.
- [24] A. C. Borges, C. Eyholzer, F. Duc et al., “Nanofibrillated cellulose composite hydrogel for the replacement of the nucleus pulposus,” *Acta Biomaterialia*, vol. 7, no. 9, pp. 3412–3421, 2011.
- [25] R. Xiong, C. Lu, Y. Wang, Z. Zhou, and X. Zhang, “Nanofibrillated cellulose as the support and reductant for the facile synthesis of $\text{Fe}_3\text{O}_4/\text{Ag}$ nanocomposites with catalytic and antibacterial activity,” *Journal of Materials Chemistry A*, vol. 1, no. 47, pp. 14910–14918, 2013.
- [26] M. Timusk, M. Järvekülg, A. Salundi et al., “Optical properties of high-performance liquid crystal-xerogel microcomposite electro-optical film,” *Journal of Materials Research*, vol. 27, no. 9, pp. 1257–1264, 2012.
- [27] B. Deepa, E. Abraham, L. Pothan, N. Cordeiro, M. Faria, and S. Thomas, “Biodegradable nanocomposite films based on sodium alginate and cellulose nanofibrils,” *Materials*, vol. 9, no. 1, pp. 50–57, 2016.
- [28] T. Wang and L. T. Drzal, “Cellulose-nanofiber-reinforced poly(lactic acid) composites prepared by a water-based approach,” *ACS Applied Materials & Interfaces*, vol. 4, no. 10, pp. 5079–5085, 2012.
- [29] S. Belbekhouche, J. Bras, G. Siqueira et al., “Water sorption behavior and gas barrier properties of cellulose whiskers and microfibrils films,” *Carbohydrate Polymers*, vol. 83, no. 4, pp. 1740–1748, 2011.
- [30] S. Tidjarat, W. Winotapun, P. Opanasopit, T. Ngawhirunpat, and T. Rojanarata, “Uniaxially aligned electrospun cellulose acetate nanofibers for thin layer chromatographic screening of hydroquinone and retinoic acid adulterated in cosmetics,” *Journal of Chromatography A*, vol. 1367, pp. 141–147, 2014.
- [31] T. W. Kim, Y. Yang, F. Li, and W. L. Kwan, “Electrical memory devices based on inorganic/organic nanocomposites,” *NPG Asia Materials*, vol. 4, no. 6, p. e18, 2012.
- [32] J. Yuan, Y. Xu, and A. H. E. Müller, “One-dimensional magnetic inorganic-organic hybrid nanomaterials,” *Chemical Society Reviews*, vol. 40, no. 2, pp. 640–655, 2011.
- [33] W.-Q. Fan, J. Feng, S.-Y. Song, Y.-Q. Lei, G.-L. Zheng, and H.-J. Zhang, “Synthesis and optical properties of europium-complex-doped inorganic/organic hybrid materials built from oxo-hydroxo organotin nano building blocks,” *Chemistry - A European Journal*, vol. 16, no. 6, pp. 1903–1910, 2010.
- [34] Q. Yao, Y. Xiong, H. Wang, C. Wang, and Q. Sun, “ MnO_2 -nanoflakes/cellulose nanofibre aerogel fabricated via ultrasonication for high-performance water desalination,” *Journal of Materials Chemistry A*, vol. 5, no. 20, pp. 9580–9590, 2017.
- [35] Y. Xiong, C. Wang, H. Wang et al., “A 3D titanate aerogel with cellulose as the adsorption-aggregator for highly efficient water purification,” *Journal of Materials Chemistry A*, vol. 5, no. 12, pp. 5813–5819, 2017.
- [36] Z. Cheng and J. Lin, “Layered organic-inorganic hybrid perovskites: structure, optical properties, film preparation, patterning and templating engineering,” *CrystEngComm*, vol. 12, no. 10, 2010.
- [37] S. Xiao, R. Gao, Y. Lu, J. Li, and Q. Sun, “Fabrication and characterization of nanofibrillated cellulose and its aerogels from natural pine needles,” *Carbohydrate Polymers*, vol. 119, no. 119, pp. 202–209, 2015.
- [38] R. Bezerra, M. Silva, A. Morais et al., “Phosphated cellulose as an efficient biomaterial for aqueous drug ranitidine removal,” *Materials*, vol. 7, no. 12, pp. 7907–7924, 2014.
- [39] N. Cai, X. Wang, D. Guo et al., “Titanium dioxide fibers prepared from two novel polytitanium precursors containing linear Ti-OH-Ti chains applied for photocatalytic degradation,” *Materials Letters*, vol. 153, pp. 191–194, 2015.
- [40] X. Liu, Y. Li, J. Yang et al., “Enhanced photocatalytic activity of CdS-decorated TiO_2 /carbon core-shell microspheres derived from microcrystalline cellulose,” *Materials*, vol. 9, no. 4, pp. 245–231, 2016.
- [41] I. Chauhan and P. Mohanty, “In situ decoration of TiO_2 nanoparticles on the surface of cellulose fibers and study of their photocatalytic and antibacterial activities,” *Cellulose*, vol. 22, no. 1, pp. 507–519, 2015.
- [42] J. Zeng, S. Liu, J. Cai, and L. Zhang, “ TiO_2 immobilized in cellulose matrix for photocatalytic degradation of phenol under weak UV light irradiation,” *The Journal of Physical Chemistry C*, vol. 114, no. 17, pp. 7806–7811, 2010.
- [43] B. Fan, S. Chen, Q. Yao, Q. Sun, and C. Jin, “Fabrication of cellulose nanofiber/ALOOH aerogel for flame retardant and thermal insulation,” *Materials*, vol. 10, no. 3, p. 311, 2017.
- [44] M. Poletto, H. Ornaghi Júnior, and A. Zattera, “Native cellulose: structure, characterization and thermal properties,” *Materials*, vol. 7, no. 9, pp. 6105–6119, 2014.
- [45] M. K. Debanath and S. Karmakar, “Study of blueshift of optical band gap in zinc oxide (ZnO) nanoparticles prepared by low-temperature wet chemical method,” *Materials Letters*, vol. 111, no. 45, pp. 116–119, 2013.
- [46] C. Aulin, J. Netrval, L. Wågberg, and T. Lindström, “Aerogels from nanofibrillated cellulose with tunable oleophobicity,” *Soft Matter*, vol. 6, no. 14, pp. 3298–3305, 2010.
- [47] X. Lang, W. Ma, C. Chen, H. Ji, and J. Zhao, “Selective aerobic oxidation mediated by TiO_2 photocatalysis,” *Accounts of Chemical Research*, vol. 47, no. 2, pp. 355–363, 2013.
- [48] N. de la Cruz, V. Romero, R. F. Dantas et al., “o-Nitrobenzaldehyde actinometry in the presence of suspended TiO_2 for photocatalytic reactors,” *Catalysis Today*, vol. 209, no. 12, pp. 209–214, 2013.
- [49] M. Y. Abdelaal and R. M. Mohamed, “Novel Pd/ TiO_2 nanocomposite prepared by modified sol-gel method for photocatalytic degradation of methylene blue dye under visible light irradiation,” *Journal of Alloys and Compounds*, vol. 576, pp. 201–207, 2013.
- [50] F. Chen, Z. Liu, Y. Liu, P. Fang, and Y. Dai, “Enhanced adsorption and photocatalytic degradation of high-concentration methylene blue on Ag_2O -modified TiO_2 -based nanosheet,” *Chemical Engineering: Journal*, vol. 221, no. 2, pp. 283–291, 2013.
- [51] A. Abbasi, D. Ghanbari, M. Salavati-Niasari, and M. Hamadian, “Photo-degradation of methylene blue: photocatalyst and magnetic investigation of Fe_2O_3 - TiO_2 nanoparticles and nanocomposites,” *Journal of Materials Science: Materials in Electronics*, vol. 27, no. 5, pp. 4800–4809, 2016.
- [52] R. Kumar, R. El-Shishtawy, and M. Barakat, “Synthesis and characterization of $\text{Ag-Ag}_2\text{O}/\text{TiO}_2$ @polypyrrole heterojunction for enhanced photocatalytic degradation of methylene blue,” *Catalysts*, vol. 6, no. 6, 2016.
- [53] D. Zhao, X. Yang, C. Chen, and X. Wang, “Enhanced photocatalytic degradation of methylene blue on multiwalled carbon nanotubes- TiO_2 ,” *Journal of Colloid and Interface Science*, vol. 398, pp. 234–239, 2013.



Hindawi
Submit your manuscripts at
www.hindawi.com

